Theor Chem Acc (2007) 118:53–65
DOI 10.1007/s00214-006-0240-z

REGULAR ARTICLE

Bosonic helium clusters doped by alkali metal cations: interaction forces and analysis of their most stable structures

F. Marinetti · E. Coccia · E. Bodo ·
F. A. Gianturco · E. Yurtsever ·
M. Yurtsever · E. Yildirim

Received: 26 October 2006 / Accepted: 24 November 2006 / Published online: 23 January 2007

Abstract Ab initio potentials are computed for alkali metal cationic partners interacting with ^{4}He and an overall many-body potential is constructed for each of the ionic dopants in helium clusters. The structures are then obtained via a genetic algorithm approach and results compared with Basin-Hopping Monte Carlo simulations. The classical arrangements are analyzed and quantum effects discussed in comparison with what has been found with Diffusion Monte Carlo calculations. Further corrections to the classical picture by including three-body forces and radial delocalization of the helium adatoms are also considered and their effects analyzed.

Keywords van der Waals clusters · Stable structures · Ionic dopants

1 Introduction

The use of ^{4}He liquid nanodroplets containing atoms between 10^3 and 10^7 provides a unique environment for the study of molecules and of molecular or atomic clusters [1–4]. Exactly because helium atoms provide the most inert solvents, the highly quantum features of these particles allow them to behave collectively as a very adaptive container for the molecular impurities. Although most of the research on doped ^{4}He droplets has focused on the rotational, vibrational and electronic spectroscopies of the impurities embedded in the droplets [1,2,5,6] as triggered by the observation of spectral shifts occurring with respect to the isolated species [1], there is also a growing interest in both photoionization and electron impact ionization experiments on doped helium droplets, on the interaction between the ensuing dopant ion and the droplet environment and the post-ionization dynamics of the ionic migration within the adaptive, microsolvating quantum fluid represented by the droplet environment [7–9]. The studies on electron impact ionization of heavier rare gases as droplets [10] suggested microscopic processes resulting in the formation of rare gas "subclusters" within the droplet with negligible fragmentation of the dopant cluster ions after ionization, a result partly confirmed by later experiments [11].

The slow migration rates of ionic dopants (mainly cationic species) are related to the marked changes of the interaction forces once a charge is localized on one of the partners (mainly on the dopant), whereby the electrostriction effects on the surrounding solvent atoms increase their density around the impurity, further ordering (localizing) their relative positioning with respect to the solvated molecule: the "snowball" model of the process [12]. It therefore becomes of interest to be able to describe the onset of such ionic interactions, their relative strength and features and the consequences which they have on the building-up of the adaptive helium partners around the specific dopant cation.

This work is dedicated to the late Nando Bernardi, an eclectic and gifted scientist and a dear friend whose early departure has left a sad void in our community.

F. Marinetti · E. Coccia · E. Bodo · F. A. Gianturco (✉)
Department of Chemistry and CNISM, University of Rome
La Sapienza, Piazzale A. Moro 5, 00185 Rome, Italy
e-mail: fa.gianturco@caspur.it

E. Yurtsever
Department of Chemistry, Koç University, Rumelifeneri
Yolu, 34450 Sariyer, Istanbul, Turkey

M. Yurtsever · E. Yildirim
Department of Chemistry, Istanbul Technical University,
34469 Maslak, Istanbul, Turkey

In the present work we have therefore started this analysis by generating an accurate, ab initio description of the potential energy curves (PECs) between alkali metal cations (Li^+, Na^+ and K^+) and a single helium atom, further computing their bound vibrational states for the J = 0 complex. We then depicted the behavior of the overall interaction within clusters of varying sizes as the one given by the sum-of-potentials approximation, i.e., as being described by the following relationship:

$$V(\mathbf{R},\mathbf{r}) = \sum_{i=1}^{n} V_{M^+-\mathrm{He}}(\mathbf{R}_i) + \sum_{j<k}^{n} V_{\mathrm{He-He}}(\mathbf{r}_{ij}) \qquad (1)$$

where we disregard for the time being the three-body (3B) effects and higher order contributions. Our earlier studies on this problem [13–15] have shown (for ionic dopants) that the 3B contributions are not negligible, while however remaining within a few percent of the total energies. Furthermore, we have also seen [13–15] that the structural observables are essentially unaffected by such corrections and therefore the results on cluster structuring evolution remain reliable even when using the potential model of Eq. (1). These points will be further addressed below in our detailed presentation of the present results.

In the following section, we shall therefore report the component PECs used as building blocks to assemble the overall interaction of Eq. (1) and their individual characteristics in terms of the bound states they support for the J = 0 configurations. Section 3 will describe in turn the optimization procedures employed to obtain classical structures of the smaller clusters and of our attempts at modeling the quantum delocalization features of the helium adatoms. Section 4 will analyze our results for the three ionic cases and discuss their most important characteristics, while Sect. 5 will finally present our conclusions.

2 The interaction potentials

For the Li^+–He potential we employed coupled-cluster (CC) ab initio calculations involving single, double and non-iteratively triple excitations [CCSD(T)], using a cc-pv5Z quality of basis set expansion [16]. The equilibrium geometry was found to be at 1.898 Å, with a dissociation energy value, D_e, of 646.168 cm^{-1}. We have discussed this potential in greater detail before [13] and therefore will not be repeating here our analysis of it. Suffice it to say that our description of that interaction turned out to be in very good agreement with earlier computational studies [17].

For the calculations of the $(NaHe)^+$–He potential we employed CC ab initio calculations involving single, double and non-iteratively triple excitations [CCSD (T)] and using again a cc-pv5Z quality of expansion [16]. The equilibrium distance was found to be at 2.232 Å, with a D_e value of 331.29 cm^{-1}. One of the most recent ab initio studies has been the one reported by Ref. [18], where the equilibrium geometry was found to be 2.324 Å with a D_e value of 329.1 cm^{-10}. We therefore see that our present findings are fairly close to the best earlier calculations. Similar calculations have also been carried out for the K^+He system: we employed the CC approach, including singles, doubles and non-iteratively triple excitations [CCSD(T)] with an aug-cc-pv5Z basis set expansion. This basis was generated by augmenting it with a large and flexible additional set with contraction of the effective core potential (ECP10MWB) [19]. For all systems examined here the basis set superposition errors were corrected by using the counterpoise method [16]. In the case of K^+He the well depth value and that of the equilibrium internuclear distance were found to be 185.5 cm^{-1} and 2.83 Å, respectively. These results are essentially coincident with an earlier calculation [20] which turns out to be the most cited paper on KHe^+: 185.4 cm^{-1} and 2.825 Å.

All these potential points were fitted by using the following analytic form:

$$V(R) = \mathrm{e}^{-\beta(R-R_0)} \sum_{k=1}^{n-1} a_k (R-R_0)^k - a_4 \frac{f(R)}{R^4} \qquad (2)$$

where the damping function $f(R)$ is given by

$$f(R) = 1 - \exp(-\beta R) \sum_{k=1}^{4} \frac{(\beta R)^4}{k!} \qquad (3)$$

the above fitting functions contain 17 parameters for each system and they can be obtained on request from the authors. The parameter a_4 has been obtained in order to yield the correct polarization potential behavior at large distances. Thus, it produced the helium atom dipole polarizability value of 1.38 a.u.

The He–He interactions within Eq. (1) were described by the best available empirical potential [21] and combined with each of the dopant-He interactions to produce the final overall interactions in each of the studied clusters.

In the three panels of Fig. 1 we report in graphical form the shapes of the three potential curves in the region of their well locations, with superimposed on them the shape and collocation of their corresponding lowest bound states. The latter were obtained by numerical integration of the nuclear Schrödinger equation [22].

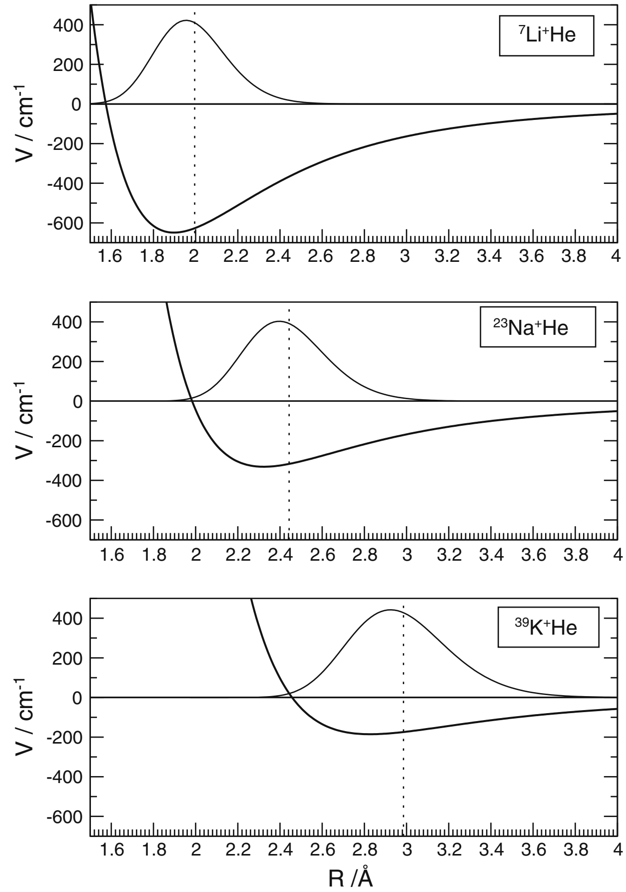

Fig. 1 Comparison of the computed potential energy curves of the present work for the three ionic potentials. The corresponding lowest bound states for J = 0 are also shown

It is interesting to note that the zero point energy (ZPE) values are rather different along the series of ionic dopants: for $(^7\mathrm{Li}^4\mathrm{He})^+$ it corresponds to 129.18 cm^{-1}, which is about 20% of the overall well depth computed for that system. On the other hand, the Na$^+$He curve produces a ZPE value of 74.09 cm^{-1}, which now corresponds to about 23% of the PEC well depth. In the case of the K$^+$He system we further see that the ZPE corresponds to 48.39 cm^{-1} which is now more than 26% of that system's well depth.

All the computed binding energies for all three potentials are given by Table 1, obtained using the fitted functions given by Eqs. (2) and (3) and by the numerical integration of Ref. [22]: all the more common isotopic variants are also given in that table. We clearly see that the ^{7}Li^{4}He ionic system supports seven bound states while the corresponding findings for Na$^+$He indicate for the latter the existence of also seven bound states, although all the top ones turn out (see table) to be very close to the dissociation limit and certainly affected by the numerical accuracy of our integration method.

Naturally, the results for the Li$^+$–He PEC of the present work are the same as those of [12] and presented there.

Finally, we see that the K$^+$He potential supports six bound states and that the top one is also very close to the dissociation limit.

As a pictorial assessment of their spatial extent, we report in Fig. 2 the locations, over the spatial range of each PEC, of the top least bound states of the three systems: for LiHe$^+$ we also report an additional state for $\nu = 7$ which is found to have a rather doubtful binding energy of 7×10^{-4} cm^{-1} and which clearly behaves as essentially a dissociative state very close to threshold.

All the outermost bound states of Fig. 2 define the range of radial values within which one He atom can still be treated as bound to the ionic core. Hence, we see that the maximum of the seventh wavefunction with Li$^+$ as a partner is located around 8 Å, while the same maximum appears around 12 Å for Na$^+$He and at a very similar value for the K$^+$He system. These features help us to see how important the specific behavior of each PES is in affecting the location of additional adatoms as the cluster grows and therefore will help us with our analysis of the ground states of the classical clusters described in the next sections.

To further see the influence of additional 3B-forces on the energetics of the clusters with more than one He adatom, we decided to carry out ab initio calculations, with the same level of theory as before, for the three trimeric ions: Li$^+$He$_2$, Na$^+$He$_2$ and K$^+$He$_2$. The

Table 1 Computed bound state energies (J = 0) for all the isotopic variants of the three potential energy curves discussed in the present work

ν	^{6}Li^{3}He	^{6}Li^{4}He	^{7}Li^{3}He	^{7}Li^{4}He	^{23}Na^{3}He	^{23}Na^{4}He	^{38}K^{3}He	^{38}K^{4}He	^{41}K^{3}He	^{41}K^{4}He
0	−504.7565	−516.3114	−507.9897	−519.9043	−248.3467	−257.2019	−130.9554	−136.9712	−131.0408	−137.0713
1	−279.0073	−303.5130	−285.7652	−311.3315	−125.5680	−143.0210	−56.3449	−66.8910	−56.4877	−67.0747
2	−131.5710	−157.1542	−138.4498	−165.6773	−53.1334	−69.6456	−18.8451	−27.2055	−18.94948	−27.3626
3	−49.7054	−68.5339	−54.5558	−75.2635	−17.6787	−28.6520	−4.2932	−8.6302	−4.3405	−8.7216
4	−13.5048	−23.5296	−15.9114	−27.5246	−3.9434	−9.2389	−0.4122	−1.7783	−0.4229	−1.8139
5	−1.9316	−5.4744	−2.6665	−7.1837	−0.3405	−1.9366		−0.1240		−0.1300
6	−0.0292	−0.5269	−0.0893	−0.9257		−0.1336				

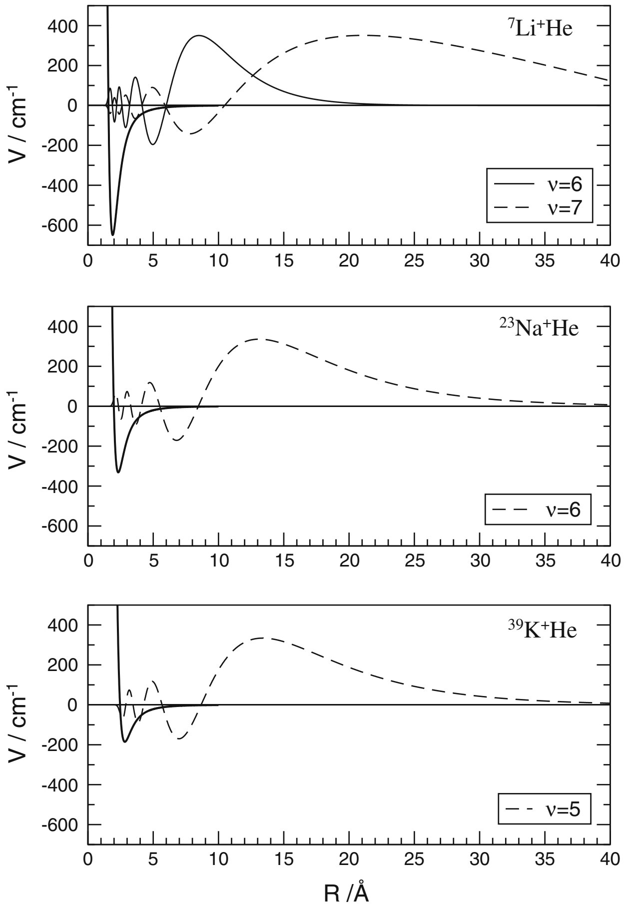

Fig. 2 Computed bound states for the topmost level in each of the ionic systems. For Li^+He an additional dissociative state very close to threshold is also shown

ab initio results for the $LiHe_2^+$ ion indicate a minimum configuration which has a bent structure with $\vartheta = 106°$ and a distance of 1.9 Å. These data are very close to the quantum results we had obtained earlier by using the sum-of-potentials approach of Eq. (1)[13]: 124° ± 24° and 2.01 Å. Furthermore, the computed binding energy is here of $-1287.23\,\mathrm{cm}^{-1}$, which is only $11\,\mathrm{cm}^{-1}$ higher than the sum-of-potential result of $-1298\,\mathrm{cm}^{-1}$. This value indicates, therefore, that for ionic partners the combined effects of "electrostriction" and "snowball" formation [23] conjure up a structural picture close to the classical one and to an overall interaction given by Eq. (1). In any case, the linear structure was found to be symmetric and very close in energy: hence it is difficult to realistically decide wether or not the most stable structure remains linear.

Similar calculations for the $NaHe_2^+$ trimer produced an ab initio linear structure ($\vartheta = 180°$) and equilibrium bond distance of 2.32 Å, not far from the value of the trimer quoted before (2.23 Å). Furthermore, the corresponding ab initio binding energy was found to be $-659.821\,\mathrm{cm}^{-1}$, which differs by only $2\,\mathrm{cm}^{-1}$ from the sum-of-potential total energy: a confirmation of the substantial validity of that model.

Finally, the ab initio calculations for the K^+He_2 ionic trimer yielded again a linear structure ($\vartheta = 180°$) for its optimal geometry and a bond distance of 2.831 Å, which does not differ much from one of the monomer found by the same level of calculation (2.827 Å). The total energy of $-367.765\,\mathrm{cm}^{-1}$ also agrees well with the sum of potential value of $-370.90\,\mathrm{cm}^{-1}$. In other words, at least for the smaller clusters, 3B effects play a rather limited role and suggest that we could employ Eq. (1) to generate spatial structures for the larger ionic clusters created via the accurate, ab initio PEC described in the present work. The methods that we shall use to generate such structures will be discussed in detail in the following section. One should keep in mind, however, that the smallness of 3B effects within dominantly linear structures (where relative distances between the two adatoms are maximized) is certainly not a surprising result.

One should further note that the overall minimum energies for all three systems of their linear or of their bent structures are very close to each other, since they chiefly differ by the long-range He–He potential. Thus, the ab initio calculations can generate either one or the other configuration depending on small changes of the basis sets or of the computational method. In any event, the optimization methods reported in the following section indicate that the classical bent structures are invariably the lowest ones in energy when the sum-of-potentials model is employed for all three ions.

3 The optimization methods

One of the crucial issues in the analysis of structural details is the reliability of classical optimization procedures for obtaining the most stable structures and the energetics of cluster formation and cluster growth in the presence of ionic dopants for a quantum solvent like helium. In reporting a comparison of such classical findings with those where the He adatoms are correctly treated as quantum objects we shall show below that the former is indeed a realistic procedure and that the classical determination of the cluster structures is able to provide significant data on ionic microsolvation.

In carrying out the classical analysis, which is the main focus of the present work, we followed two distinct optimization processes, briefly outlined in two subsections below. We further included three-body effects on the energetics and a quantum representation of radial delocalization of adatoms: both corrections to the classical picture of the microsolvation are also outlined below.

3.1 The genetic algorithm approach

In order to carry out structural optimization we use a method based on the well-known genetic algorithm [24,25], a procedure which can provide a reasonably fast way to find the minima for a general multidimensional function as that given by the present overall potential. The method follows closely the scheme we recently reviewed in [26] whereby a generic i-th individual, in our case a single geometric structure with a given energy, is described by the $3N$ Cartesian coordinates of the N atoms ($\{x_j^i\}, j = 1 : 3N$), plus a further set of strategy parameters ($\{\eta_j^i\}, j = 1 : 3N$), which are standard deviations of a Gaussian function centered on each coordinate. The starting population of M (randomly chosen) individuals constitutes the first parents set and such a set evolves according to an evolution law that generates a new population of offsprings:

$$x_j^{i'} = x_j^i + \eta_j^i N_j(0,1)\Delta \tag{4}$$

$$\eta_j^{i'} = \eta_j^i \exp\left[\tau' N(0,1) + \tau N_j(0,1)\right] \tag{5}$$

where $N(0,1)$ and N_j (0,1) are standard Gaussian random numbers, the two parameters τ and τ' are respectively equal to $(\sqrt{2\sqrt{3N}})^{-1}$ and $(\sqrt{6N})^{-1}$ and Δ is a displacement factor that increases the resolution power. The union of the parents and the offsprings provides a population made of $2M$ individuals whose members challenge now a number q of randomly chosen opponents. The winner of each challenge is the individual with the lower energy value, and it scores one point. The best M individuals are then becoming parents for the next iteration and so on.

When convergence is reached, within a preselected energy "width", the best structure is entered as input in an outer cycle where it randomly generates the next number of M structures that are characterized by the following data:

$$x_j^{i'} = x_j^i + N_j(0,1)\Delta \tag{6}$$

$$\eta_j^i = 1.0 \tag{7}$$

and which now yield a new set of parents. These are in turn employed as input in the procedure we have described above and they perform a further optimization by producing a new, energetically improved, structure. At the end of each outer cycle the value of Δ is decreased in order to obtain a better resolution during selection and the procedure ends when the resolution value is under the selected tolerance threshold for the energy.

3.2 Basin–Hopping Monte Carlo

Basin Hopping Monte Carlo (BMHC) is a global optimization algorithm which combines a conjugate gradient optimization with a large-step Monte Carlo simulation [27,28].

For large and weakly bound clusters, in fact, the search for a global minimum is very difficult because of the exponentially large number of local minima which may also be separated by large barriers along their phase space trajectory. In order to overcome these barriers, large trial moves are introduced at equal intervals and are accepted or rejected with Boltzmann probabilities as in the importance sampling Monte Carlo [29] procedures. After a sufficient number of moves is attempted, a conjugate gradient optimization is applied to locate a minimum and to form a data base of such local minima. This method has two adjustable control parameters which are given by the temperature and the amplitude of atomic displacements which are used to obtain optimal results.

For complicated potential-energy-surfaces (PES), finding the global minimum from a single trajectory is a difficult task even for sophisticated methods such as the genetic algorithms discussed in the previous section. In particular, escaping from a funnel in the PES may require either a systematic formation of a database of minima or running multiple trajectories to achieve a nearly complete span of the phase space. For the study of ionic dopants as in the present situation, there is an additional complication given by the fact that, even though He–He interaction is very weak compared to that of M^+–He, it still dominates the interactions when the helium atom is far away from the ion. Consequently, optimization algorithms may spend a great deal of time trying to optimize the system total energy by optimizing He–He interactions. In this work we have applied a growth scheme to overcome this problem whereby each new cluster is generated by randomly placing a helium atom in the vicinity of the previous cluster. This atom is placed into the outermost shell with two randomly selected angular coordinates. Minima located from these structures are added to a database and, after running a sufficient number of trajectories, the lowest energy structure is selected to generate the next one. We have used a simple convergence criterion where it is assumed that the global minimum is found if three new sequences do not produce lower energy structures. In this work 100 such sequences are generated for clusters of size up to He_{70} [30].

3.3 Modeling 3B corrections

As mentioned in the introduction, the prescription (1) for the total interaction disregards the effects coming from three-body (3B) contributions to the potential on the grounds that all our earlier studies had found them to be small in comparison with the microaggregate total energies [13,14].

In the present study, and in our recent analysis of a molecular cation as a dopant [26], we further improve on Eq. (1) by adding the largest 3B contribution for the cationic dopant which interacts with He atoms. This contribution is given by the coupling between the dipoles induced on the helium atoms that are oriented in such a way as to minimize their repulsive interactions. The analytical formula for this term is very simple once we consider a point charge located at the center of mass of the molecular ion and is given by

$$V_{3B}(r_i, r_j) = -\frac{\mu\mu'}{r_{ij}^3}(2\cos\theta_i\cos\theta_j - \sin\theta_i\sin\theta_j) \tag{8}$$

where θ_i and θ_j are the angles between the dipoles and the line joining them, and where the induced dipole moments μ and μ' at distance r from the ion can be evaluated with the well known formula: $\mu = \alpha/r^2$.

Using the above correction term for all induced dipoles in each cluster, we have thus corrected both the total energy values and the radial distributions in each cluster: we shall see below that such dominant corrections do not really alter the general picture of the spatial arrangements which are obtained using only the sum-of-potentials approach.

3.4 Modeling the quantum distributions

In order to improve on the classical analysis of the structures by including to same extent the additional effects of quantum delocalization pertaining to the solvent atoms, we have introduced radial distributions associated with the latter partners and employed them to modify the initial “balls and sticks” picture obtained from the optimization algorithm.

For an atom in the cluster, the probability of being at a distance between r and $r+\mathrm{d}r$ is given by $P(r) = \rho(r)\mathrm{d}r$, where $\rho(r)$ is the required radial distribution function. It is possible to build such a function for the helium atoms surrounding the cationic dopant by taking advantage of the data already provided by the optimization procedure.

For an N-atoms cluster, the shape of the function $\rho(r)$ can be, in fact, approximated by the expression:

$$\rho(r) = \sum_{i=1}^{N} \frac{1}{\sqrt{(2\pi\sigma_i)}} \exp\left(-\frac{(r-\bar{r}_i)^2}{2\sigma_i}\right) \tag{9}$$

where $\bar{r}_i$ is the i-th atom distance after the optimization and σ_i is the standard deviation of the ith atom distance obtained with the propagation on the strategy parameter η_i multiplied by Δ. In this distribution function each atom stays in a position centered in $\bar{r}_i$ and is distributed according to a Gaussian with a standard deviation equal to the method sensitivity. The radial distribution is then normalized to the number of atoms in the cluster under consideration.

In order to provide an estimate of the possible quantum distribution, we can approximate the real quantum dispersion of the helium atoms bound to the dopant by arbitrarily setting the value of the standard deviation equal to the half width of a known quantum distribution multiplied by the strategy parameter η_i. In this way we obtain a simulated “quantum spreading” of the helium atoms in the cluster. The quantum solution we have chosen is that associated with the ground state wavefunctions of $\mathrm{M^+He}$ pairs already computed by us in the previous section.

We have focused on radial delocalization because our earlier work on cationic dopants [13,15] has already shown that angular delocalizations are markedly reduced and therefore the corresponding cluster structures are much more rigid to bending than their neutrally doped counterparts.

4 Discussion of results

4.1 The energy landscapes

The first quantities which we have tried to extract from our calculations involve the relative energetics of the cluster stabilizations and the progress along the growth process of the evaporative energetics, i.e., the energy required to evaporate one solvent atom from a cluster of a given size.

Both optimization procedures were followed in the calculations as it is important to establish the internal consistency of the methods. The behavior of the total binding energies as a function of cluster size is reported by Fig. 3, where the dots indicate the genetic algorithm (GeCO) results while the solid lines report the values given by the Basin Hopping (BH) procedure. The following comments could be made:

1. All three systems show a clear change of slope at some small cluster size, the latter being around $n = 6$

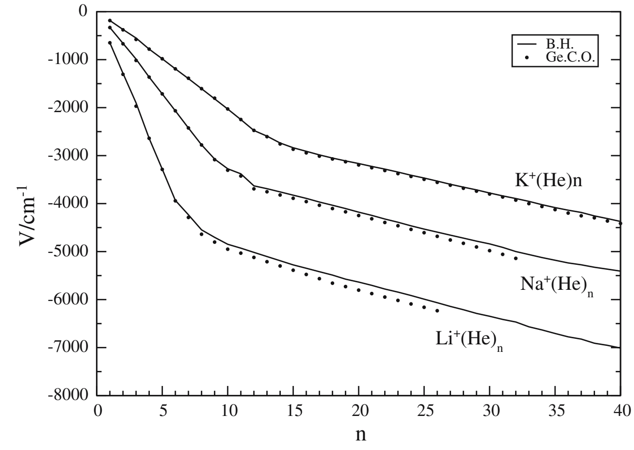

Fig. 3 Computed total binding energies (sum-of-potentials model) for clusters containing Li^+ (*bottom*), Na^+ (*middle*) and K^+ (*top*) cations, as a function of number of He adatoms. Energies in cm^{-1}. *Solid line* Basin–Hopping method (BH); *dots* Genetic algorithm results

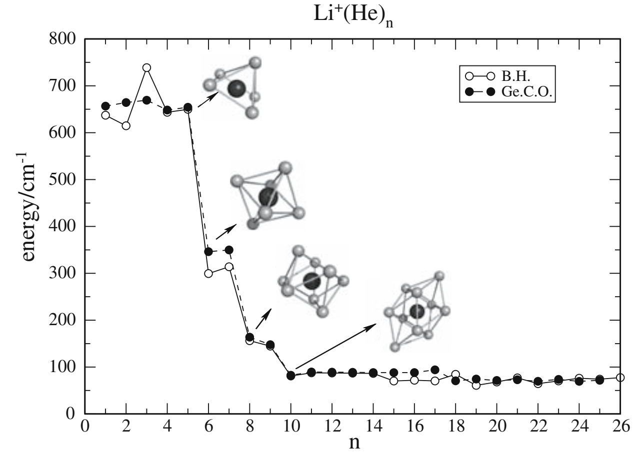

Fig. 4 Computed evaporation energies (cm^{-1}) for clusters containing the lithium cation as a dopant. Both Basin-Hopping (*open circles*) and Genetic algorithm (*filled-in circles*) are shown (in units of cm^{-1})

for Li^+, around $n = 8$ for Na^+ and around $n = 12$ for K^+.

2. The slopes of the energy n-dependence for all three clusters beyond those structural transitions remain fairly constant and indicate that the growth energetics does not go through marked "shell" formation discontinuities.

A more detailed description of what goes on as the cluster size increases could be gathered from the behavior of the evaporative energies of single adatoms reported for the three systems in Figs. 4, 5 and 6. We give in each of them the results obtained via the BH procedure (open circles) and GeCO procedure (filled-in circles), using the following equation

$$\Delta E(n) = V(n) - V(n+1) \tag{10}$$

The results for the lithium cationic dopant show again reassuring similarities between BH and GeCO calculations, with more marked oscillations for the former within the first six adatoms than what occurs for the latter. These differences may perhaps be due to unconverged bias selection in the walker population employed during the MC calculations of the BH approach: they appear in fact for all three cationic calculations, as we shall see below.

The GeCO results, in fact, are more in keeping with our recent Diffusion Monte Carlo calculations (DMC) on the same systems and with the same approach [30], where we found that the single-atom evaporation energies did not change much along the first shell of the three systems. From Fig. 4 we further see that the pyramidal structure for $n = 5$ completes an internal shell of essentially equivalent atoms which cause a sort of structural transition to the octahedral structure of the $n = 6$ cluster, for which the single-atom evaporative energies drop by almost half their previous values.

A further structural transition occurs for another "regular" solid with $n = 8$, where we see that the binding energies for each adatom now drop to one third of their previous values.

The subsequent attainment of the double pyramidal structure for $n = 10$ appears to close the first shell of the cluster since the evaporation energies do not change in any marked way when extending the cluster size from 10 to 26. In other words, we can say that the Li^+-containing clusters, within a classical picture, appear to complete their first shell for $n = 10$ but reach a regular, solid-like structure already with the octahedral configuration of $n = 6$. This point will be the object of further discussion when we shall compare below some of these findings with their quantum counterparts.

The corresponding calculations for the sodium-containing clusters are reported by Fig. 5, where we also show pictorially the most significant spatial structures of the doped clusters.

In the case of Na^+ we deal with a larger cation (see potential curves in Fig. 1) and one for which the interaction with the He adatoms is weaker than in the Li^+ case. Thus, we see that the GeCO calculations extend the energetic equivalence of the surrounding atoms up to $n = 7$ structure, with a marked drop in evaporative energy for $n = 10$. However, we see that the addition of one more atom in the $n = 11$ case now expands the cluster to the irregular structure shown in the figure

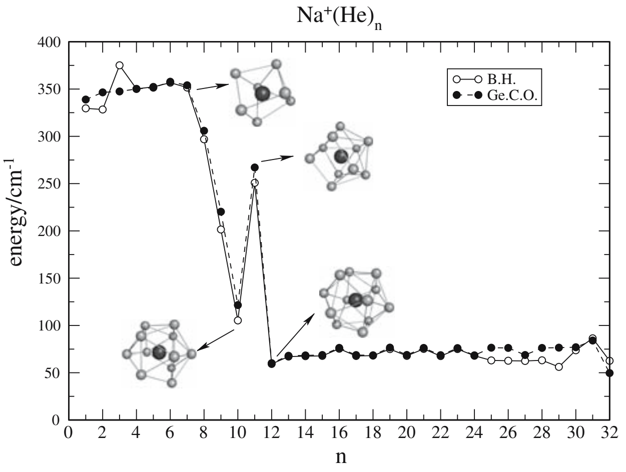

Fig. 5 Same calculations as those of Fig. 4 but for the case of the cationic sodium as a dopant. See main text for details

and therefore forces an increase of the less-screened adatoms binding energies with respect to the previous, more regular, minimum configuration. The latter further drops to an even lower value when the first shell is completed in the $n = 12$ regular "solid" shown in the figure for that cluster size. From that size we see that the evaporative energies do not change much along the series and the present calculations therefore confirm the dominance of He–He interaction effects as the clusters grow in size. Finally, we see once more small differences between BH and GeCO calculations in the two extreme situations of a few He atoms and of the larger clusters, while they both provide the same picture for the overall energetic behavior of the $Na^+(He)_n$ clusters.

The results for the $K^+(He)_n$ clusters are reported by Fig. 6 and were also described earlier by our work with the BH approach only [30]. The larger cationic size and the reduced binding energy for a single He exhibited by this system with respect to the previous ones is causing once more changes in the behavior of the evaporative energies.

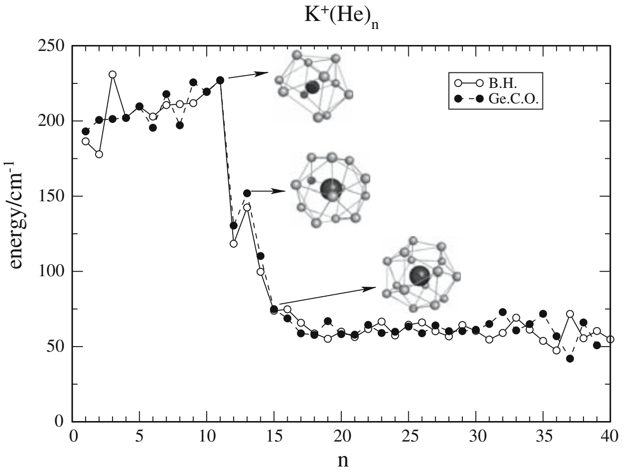

Fig. 6 Computed evaporative energies (single atom) for K^+-containing clusters. See both Fig. 4 and the main text for further details

Thus, we see that the energetic equivalence in the adatoms of the smaller clusters is more difficult to attain: each new addition, in fact, modifies the previous interactions with the central cation and therefore prevents the clearer equivalence of such quantities shown by Li^+ and Na^+. However, the first subshell is clearly completed by $n = 10$, where a structural transition is seen to occur and where the evaporative, single atom energy drops to half their initial energy value. The intermediate "expansion" shown by the sodium-containing clusters occurs here for $n = 12$ while the presence of a shell completion seems to take place around $n = 14$. We also see, however, that the energy values for larger clusters is not as clear-cut as before since the evaporative energies oscillate quite distinctly around the $50\,\mathrm{cm}^{-1}$ average value across the range of the larger clusters.

These differences between clusters could be better appreciated by comparing the evaporative energy values obtained with the GeCO calculations as shown by Fig. 7.

One clearly sees in that figure at least three interesting comparative features among the clusters:

1. The evaporation energies of the smaller clusters up to their first structural transitions are strongly dominated by the M^+–He potentials and therefore clearly scale from Li^+ to K^+ according to the relative strength of their interactions.

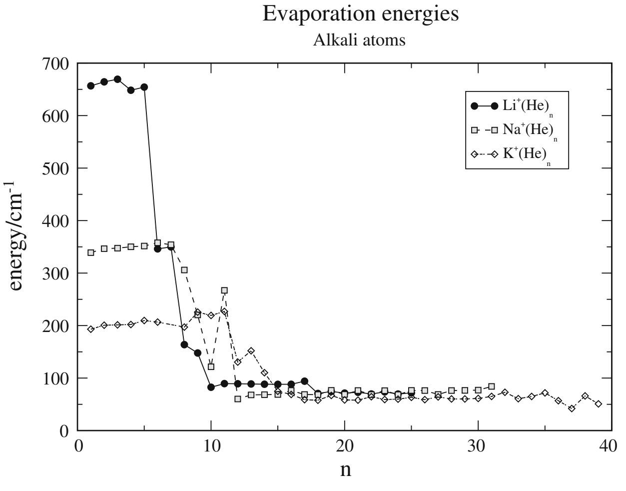

Fig. 7 Computed single-particle evaporation energies along the cluster growth and for the three different cationic dopant discussed in the present work. The results are from the genetic algorithm approach

2. The size of the central cation increases from Li^+ to K^+ and therefore we see that the number of equivalent values of evaporation energies before the transitions increase from L_i^+ ($n = 5$) to Na^+ ($n = 7$) to K^+ ($n = 11$).
3. After the structural transitions occur upon the completion of the first shells, all different sizes for the three different cations, we see that the values of the "asymptotic" evaporative energies are nearly the same for all doped clusters: they chiefly depend on the He–He interaction because of the occurrence of a nearly full screening of the central dopant.

4.2 3B- and quantum corrections

We have mentioned in the previous section that we included the 3B-correction to the sum-of-potentials scheme by using the dominant induced dipole forces and also modeled the radial broadening due to quantum delocalization by including a parametric correction taken from the quantum bound states of the monomeric complex.

The effects of such modifications on the classical calculations could be appreciated by looking at the results of Fig. 8, where we report the radial distributions of the first group of adatoms in two different clusters as listed in each panel. We see clearly the broadening effect by the quantum simulation and the spatial shifts of the distributions which, in these specific cases, are seen as increasing because of the changes on the initial repulsions between solvent atoms. The overall shape is, however, left fairly unchanged from that of the simpler calculations without 3B corrections, thus confirming the realistic qualities of the structures obtained without including 3B forces in the clusters doped by positive ions.

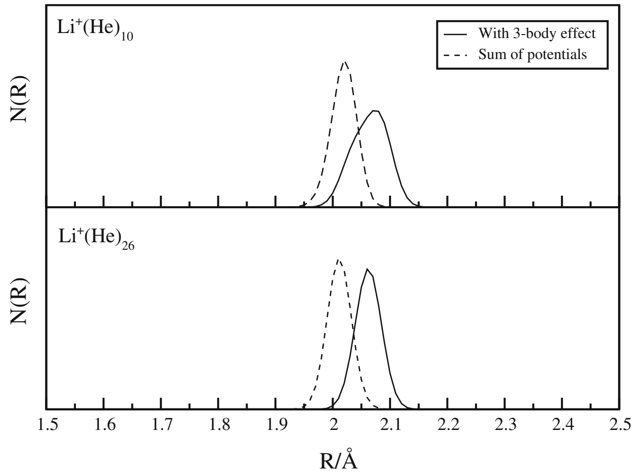

Fig. 8 Computed radial distributions for lithium-containing clusters and obtained with and without the inclusion of 3B forces. Two different cluster sizes are shown in the panels

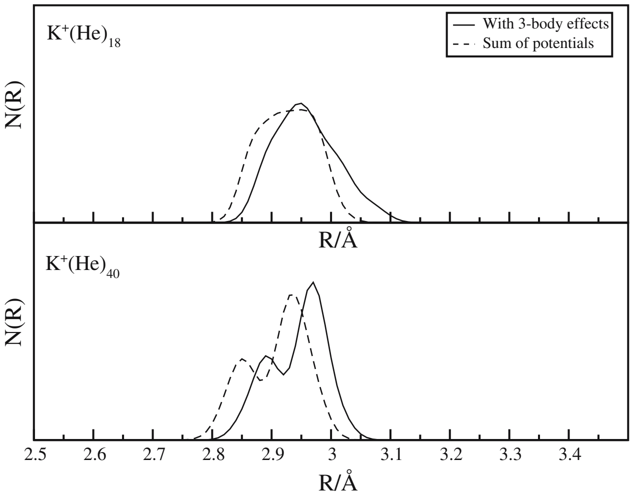

Fig. 9 Same calculations as those given by Fig. 8, this time however including K^+ as the dopant species

The same type of results are obtained when one moves to the sodium cation as a solvated impurity and therefore we shall not repeat for them the same analysis as before. The further passage to potassium-containing clusters also follows the same qualitative scaling, as can be appreciated from the data reported by Fig. 9.

The two clusters shown in that figure are also fairly large and clearly exhibit the broadening of the adatom densities already seen in Fig. 8. The area under the single region shown in the upper panel corresponds to 15 adatoms, and the more structured area below also indicates the overall presence of 15 ^{4}He adatom contributions. Both distributions, however, indicate a rather marginal effect from 3B corrections and clearly support once more the realism of using sum-of-potentials to describe the medium-to-large ionic clusters. An even more telling comparison is given by the three panels of Fig. 10, where three different clusters, with different sizes, are reported. We show there the broadened distributions when the quantum radial corrections are included for larger clusters and are compared with the radial distributions from the classical calculations.

It is interesting to note that the quantum broadening of the classical distributions (as given by all the shaded areas) follows the general structures of the classical peaks but provides a picture where the individual adatoms are much more uniformly "spread" around the central dopants. The effect of creating an increasingly unstructured spread is becoming more evident as one moves from Li^+ to K^+ as central dopants: the reduced M^+–He interaction, in fact, allows less marked snowballing and "electrostriction" features to be present in the cluster. This point will be further discussed below.

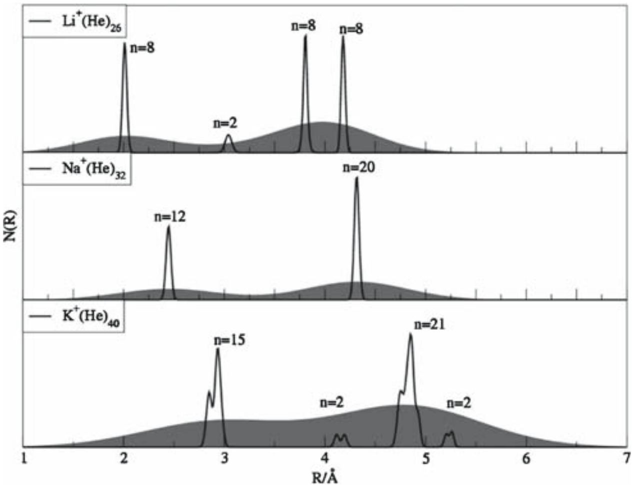

Fig. 10 Computed radial distributions for Li$^+$-containing (*upper panel*), Na$^+$-doped (*medium panel*) and K$^+$-solvated (*lower panel*) clusters of ^{4}He of different sized. The *solid curves* describe the classical distributions while the *shaded* areas include the quantum broadening for each of the peaks

The reduction of "solid-like" features when quantum effects are introduced (quantum "melting") could also be appreciated pictorially in relation to the overall strength of the monomeric interaction potentials. The results shown by Fig. 11, in fact, report the radial distributions for one of the larger lithium-containing clusters, the $n = 76$ cluster.

We see that the initial shell of ten adatoms effectively screens the central cation and shows a marked "electrostriction" effect in the sense that the most structured solvent atoms move to the bottom of the potential wells, as indicated in that picture. On the other hand, as one moves outside that shell to the more equivalent ensemble of He atoms (see for their energies the data of Fig. 7) one sees that, even classically, they get distributed over a very broad range of distances while the quantum correction shows a more "liquid-like" situation whereby all the external He atoms are evenly distributed around the central dopant with little clear structuring of their collocations.

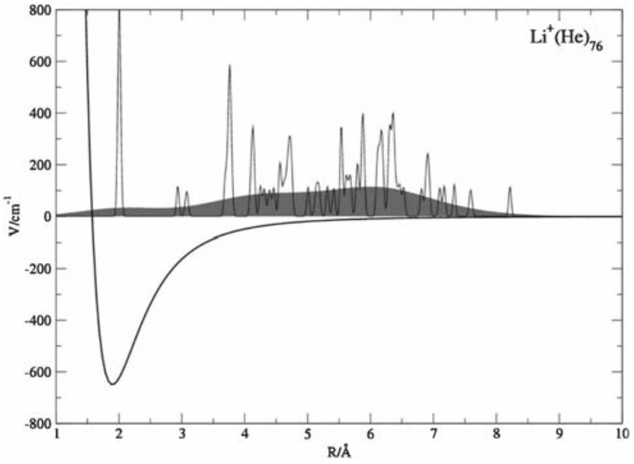

Fig. 11 Computed radial distributions from classical (*solid lines and peaks*) and quantum (*shaded area*) distributions of the He adatoms. The three closest peaks correspond to the $n = 10$ cluster

4.3 Classical and quantum densities

One of the issues when discussing the use of classical methods for the description of He-containing clusters is obviously the role played by the quantum properties of this non-classical solvent, chiefly the role of zero-point-energy (ZPE) and of spatial delocalization of the adatoms.

Our experience with ionic impurities, however [13–15], indicates that the two main consequences of charge localization onto the central cationic dopant within the cluster, i.e., that of "electrostriction" (or solvent atom crowding of the cation) and of "snowballing" (or the formation of solid-like structures around the core) [3,23], actively condition the adatoms behavior and make them more localized in space and more regularly placed around the ion. In other words, the quantum "melting" of the solvent occurs away from the central cation and after the structural transition one sees upon completion of the first shell around the dopant.

To reinforce more specifically the above findings, we have carried out quantum structural calculations for the same systems discussed here, using the same interaction potentials as those given in the initial sections of the present paper, and employed a variational Monte Carlo (VMC) procedure followed by a diffusion Monte Carlo (DMC) calculation. The details of the method and the general findings of these calculations will be reported elsewhere [31] and therefore will not be repeated here.

What we show in Fig. 12 is a very telling comparison between classical and quantum description of a "regular" cluster with Li$^+$ as a dopant. In the upper panel of the figure we project the classical locations of the six atoms once we fix the position of one of them as being along the reference z-axis originating from the dopant ion, while a second one is employed to define the xz plane. The plane shown is that given by the (ϑ, φ) polar angles and we project onto it the six adatoms represented by dots qualitatively including the delocalization width mentioned before and located with respect to the reference He atom along the axis. Because of its being a projection of the sphere onto a plane, the reference atom along the z axis arbitrarily appears on the lower-right part of the projection in terms of φ-angle value. One clearly detects, however, the regularity of the structure and the marked presence of localized densities for the adatoms.

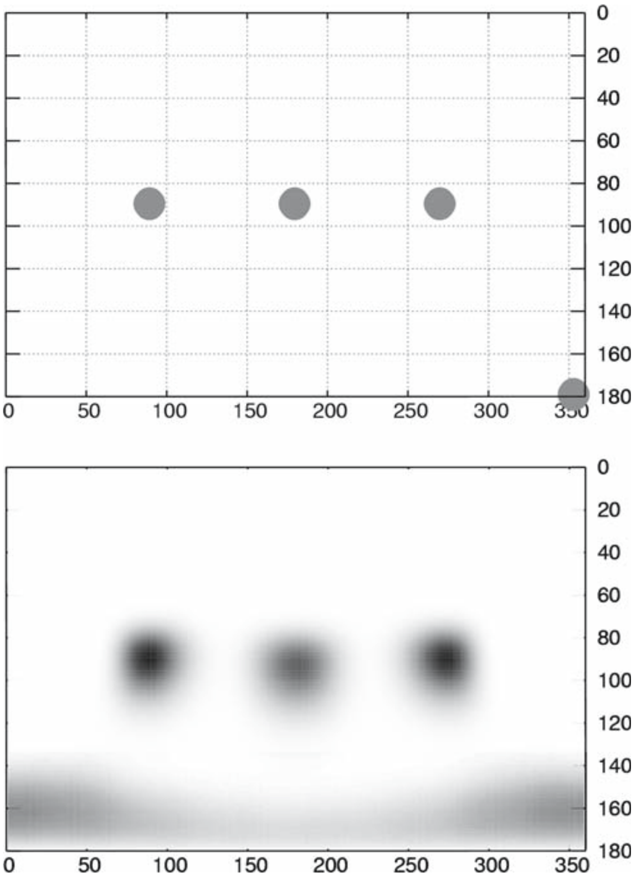

Fig. 12 Computed He–He densities correlated to a reference He atom along the z axis originating from the cationic dopant. The correlated densities are projected onto the (ϑ, φ) plane of the polar coordinates Li^+ cationic core. The ordinates report the ϑ angles

The corresponding quantum results are given in the lower panel of the same figure, where the quantum equivalence of the six adatoms transforms the undefined φ-value on the lower-right of the upper panel, seen in the figure, into a broadly given density along the whole range of the φ-angle. Apart from this difference, however, we clearly see the remarkable similarities between the two patterns: the quantum densities are obviously more "blurred" than the classical ones but they unequivocally show the presence of regular, solid-like structuring of the quantum solvent in the neighborhood of the dopant and its strong similarity with the classical picture of the upper panel.

The corresponding results for the Na^+ cation are given for a larger cluster, that for $n = 12$, in the two panels of Fig. 13.

We clearly see in both panels the combined effect of an increased compactness of the quantum adatoms (electrostriction) and of the regular locations of their densities surrounding the central cation (snowballing). Here again the undefined φ values for its quantum density and the arbitrary location of a preselected φ value in the case of the classical calculations of the upper panel are present.

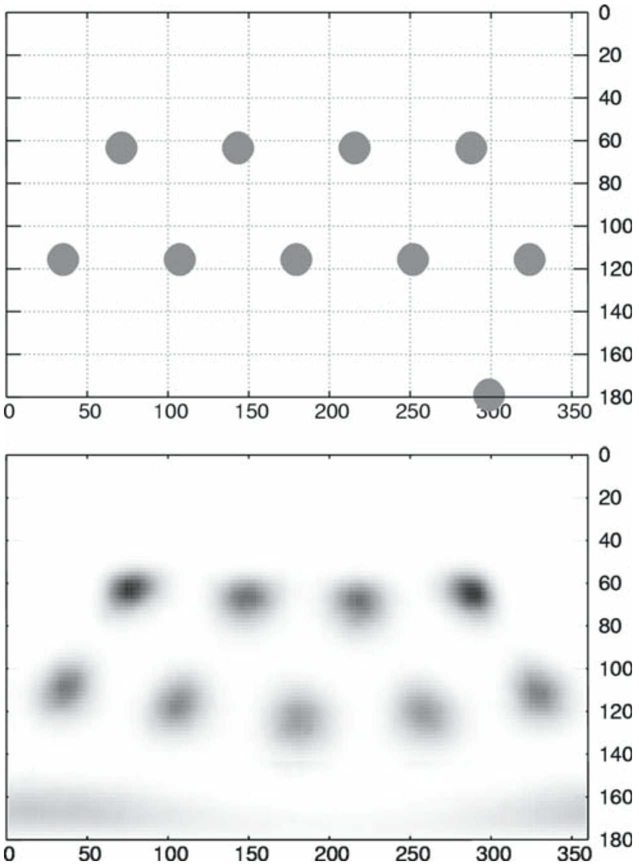

Fig. 13 Same as Fig. 12, but for the cluster with $n = 12$ and having Na^+ as the doping cation

The similar results for the K^+ impurities are presented by the two panels given in Fig. 14, where we also see the positioning at (200,180) of the He atom placed on the reference z-axis perpendicular to the projection plane.

Because of the reduction of the strength of the interaction in the case of K^+, and because of the larger size of the first surrounding shell, we see here an even more evident "blurring" of the quantum densities at regular positions: the regularity of the locations of the adatoms is however still very clear and the occurrence of the "snowball" effect also confirmed in our third cationic system.

Once we have established above the substantial equivalence of the classical and quantum pictures in the description of the energetically lowest configurations for each cluster, it is instructive to analyze the growth process by looking at the corresponding optimal configurations as provided by the present classical calculations from the GeCO method.

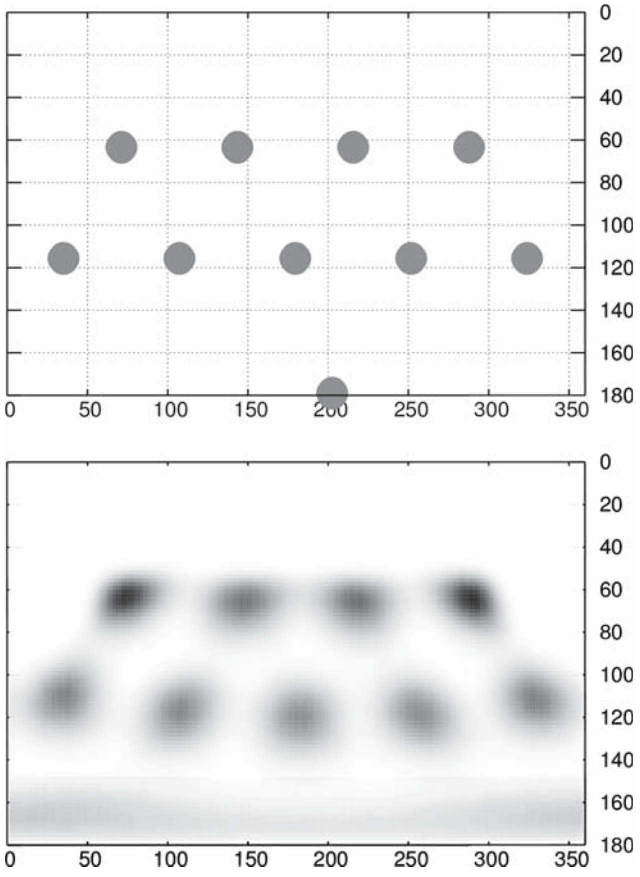

Fig. 14 Same calculations as those of Fig. 13 but involving the potassium cation as central dopant

The results of Fig. 15, which refer to Na^+ as a dopant, show the formation of a series of compact structures for n from 1 to 7, where all the atoms "see" very strongly the ionic potential, followed by a series of more open structures where the screening effects reduce the individual binding (see data of Fig. 7) until the structural transition completes the first shell for $n = 12$, with the formation of a regular, solid-like structure surrounding the cationic impurity.

The similar results for the clusters which contain the potassium ion as a dopant are shown in Fig. 16, where the effect of the reduced strength of the ionic interaction when going from $Na^+(He)_n$ to $K^+(He)_n$ is once more underscored. We see, in fact, that the system exhibits an energetic sequence that comes from the interplay between direct ionic binding and screening from fellow He atoms as the clusters become larger and at times less compact. Thus, up to $n = 9$ the binding energies remain fairly equivalent, while for $n = 10$, 11 and 12 the regular structures are seen to be less compact and therefore the individual evaporation energies increase (as shown by Fig. 7). On the other hand, the following clusters ($n = 13$, 14, 15) complete the first shell, increase the compactness of the aggregates and show reduced binding energies up to the structural transition for $n = 15$.

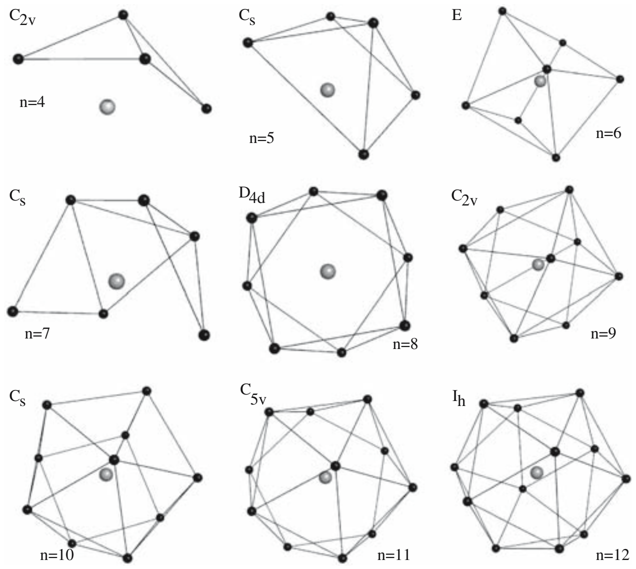

Fig. 15 Classical configurations of lowest energy for the $Na^+(He)$ for n values clusters obtained from the genetic algorithm and plotted up to the completion of the first full shell ($n = 12$)

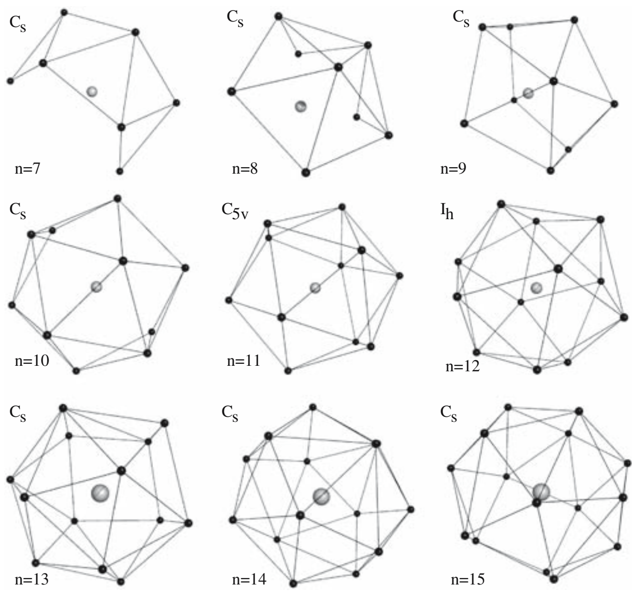

Fig. 16 Same calculations as those of Fig. 15 but for the K^+ cationic impurity with shell structuring up to $n = 15$

5 Present conclusions

In the present work we have discussed in some detail the energy landscapes and the structural features of small ^4He clusters containing ionic atoms like Li^+, Na^+ and K^+.

The interaction forces have been obtained very accurately from highly correlated ab initio calculations and have been numerically fitted to yield general functional forms for both the M^+–He and He–He interactions, the latter being obtained from earlier work on that system [21]. The full potentials have been described within the sum-of-potentials approximation and further corrected by including the dominant 3B dipole-dipole contributions: the latter were found to produce rather small effects on the cluster structures and energetics.

The quantum delocalization of this special solvent atoms has been introduced both empirically and accurately via DMC methods and shown to be strongly reduced for these ionic "solutions" where both the "electrostriction" and "snowball" effects are important and suggest the general reliability of a classical description.

The many existing structures within each cluster have been optimized using the genetic algorithm and the Basin–Hopping procedures described in Sect. 2 and the sequences of cluster growth have been analyzed within each cationic species.

The stronger interaction for the $Li^+(He)_n$ small clusters is seen to cause a structural transition around $n = 10$, beyond which the He–He interactions dominate the cluster energetics. Due to the reduced strengths of the ionic potentials of Na^+ and K^+, and because of the larger sizes of their minimum structures, one sees that the same structural transitions occur at $n = 12$ for $Na^+(He)_n$ and at $n = 15$ for $K^+(He)_n$. Beyond this size of clusters, the structures resume marked spatial delocalization of solvent atoms and are dominated by He–He potentials.

The present study therefore allows us to draw a series of both qualitative and quantitative conclusions on the energetics and on the structural features of microsolvation processes in the presence of ionic interactions and within a quantum solvent. More detailed studies from fully quantum treatments will be presented elsewhere [31].

Acknowledgments The financial support of the Italian Ministry for Research (MUIR), the University of Rome Research Committee, the European Network COMOL no. HPRN-CT-2002-00290 and the Agnelli Foundation are gratefully acknowledged.

References

1. Toennies JP, Vilesov AF (1998) Ann Rev Phys Chem 49:1
2. Toennies JP, Vilesov AF (2004) Angew Chem Int Ed 43:2622
3. Stienkemeier F, Vilesov AF (2001) J Chem Phys 115:1019
4. Nauta K, Moore DT, Miller RE (1999) Faraday Discuss 113:261
5. Scheidemann A, Shilling B, Toennies JP (1993) J Phys Chem 97:2128
6. Callegari C, Lehmann KK, Schmied R, Scoles G (2001) J Chem Phys 115:10090
7. Callicoat BE, Mar DD, Apkarian VA, Janda KC (1996) J Chem Phys 105:7872
8. Loginov E, Rossi D, Drabbels M (2005) Phys Rev Lett 95:163401
9. Kim JH, Peterka DS, Wang CC, Neumark DM (2000) J Chem Phys 124:214301
10. Lewerenz M, Schilling B, Toennies JP (1995) J Chem Phys 102:8191
11. Ruchti T, Callicoat BE, Janda KC (2000) Phys Chem Chem Phys 2:4075
12. Bodo E, Yurtsever E, Yurtsever M, Gianturco FA (2006) J Chem Phys 124:074320
13. Sebastianelli F, Baccarelli I, Di Paola C, Bodo E, Gianturco FA, Yurtsever M (2005) J Chem Phys 1:1045
14. Bodo E, Sebastianelli F, Gianturco FA, Pino I (2005) J Phys Chem A 109:4252
15. Sebastianelli F, Bodo E, Di Paola C, Baccarelli I, Gianturco FA, Yurtsever M (2006) J Comput Mater Sci 35:261
16. Werner H-J, Knowles PJ et al. www.molpro.net
17. Soldan P, Lee EPF, Lozeille J, Murrell JN, Wright TG (2001) J Chem Phys 343:429
18. Viehland LA, Lozeille J, Soldan P, Lee EPF, Wright TG (2003) J Chem Phys 119:3729
19. Leininger T, Nicklass A, Kehle W, Stoll H, Dolg M, Bergner A (1996) Chem Phys Lett 255:274
20. Viehland LA, Lozeille J, Soldan P, Lee EPF, Wright TG (2004) J Chem Phys 121:341
21. Tang KT, Toennies JP (2003) J Chem Phys 118:4976
22. LeRoy RJ (2000) University of Waterloo, Chemical Physics Research Report no. cp-555R
23. Galli DE, Buzzacchi M, Reatto L (2001) J Chem Phys 115:10239
24. Bäck T, Schwefel H-P (1993) Evol Comp 1:1
25. Iwamatsu M (2001) Comp Phys Comm 142:214
26. Marinetti F, Bodo E, Gianturco FA (2006) Chem Phys Chem (in press)
27. Doyle JPK, Wales DJ (1997) J Phys Chem A 101:5111
28. Calvo F, Yurtsever E (2004) Phys Rev B 70:045423
29. Lester WA, Hammond BL (1990) Ann Rev Phys Chem 41:283
30. Yurtsever E, Yildirim E, Yurtsever M, Bodo E, Gianturco FA (2006) Eur Phys J D (in press)
31. Coccia E, Marinetti F, Bodo E, Gianturco FA, Yurtsever E, Yildirim E, Yurtsever M (2006) J Chem Phys (Submitted)